CARBON 94 (2015) 91–100

Available at www.sciencedirect.com

ScienceDirect

journal homepage: www.elsevier.com/locate/carbon

Hexamolybdenum clusters supported on graphene oxide: Visible-light induced photocatalytic reduction of carbon dioxide into methanol

Pawan Kumar [a], *Harshal P. Mungse* [a], *Stéphane Cordier* [b], *Rabah Boukherroub* [c], *Om P. Khatri* [a], *Suman L. Jain* [a,*]

[a] *Chemical Sciences Division, CSIR-Indian Institute of Petroleum, Dehradun 248005, India*

[b] *Institut des Sciences Chimiques de Rennes, UMR 6226 UR1-CNRS, Université de Rennes 1, Campus de Beaulieu, 35042 Rennes Cedex, France*

[c] *Institut d'Electronique, de Microélectronique et de Nanotechnologie (IEMN), UMR CNRS 8520, Université Lille 1, Avenue Poincaré – BP 60069, 59652 Villeneuve d'Ascq, France*

ARTICLE INFO

Article history:
Received 24 February 2015
Accepted 13 June 2015
Available online 19 June 2015

ABSTRACT

Hexamolybdenum (Mo_6) cluster-based compounds namely $Cs_2Mo_6Br^i_8Br^a_6$ and $(TBA)_2Mo_6Br^i_8Br^a_6$ (TBA = tetrabutylammonium) were immobilized on graphene oxide (GO) nanosheets by taking advantage of the high lability of the apical bromide ions with oxygen-functionalities of GO nanosheets. The loading of Mo_6 clusters on GO nanosheets was probed by Fourier-transform infrared (FTIR) spectroscopy, X-ray photoelectron spectroscopy (XPS), high resolution transmission electron microscopy (HRTEM) and elemental mapping analyses. The developed GO-$Cs_2Mo_6Br^i_8Br^a_x$ and GO-$(TBA)_2Mo_6Br^i_8Br^a_x$ composites were then used as heterogeneous photocatalysts for the reduction of CO_2 under visible light irradiation. After 24 h visible light illumination, the yield of methanol was found to be 1644 and 1294 μmol g^{-1} cat for GO-$Cs_2Mo_6Br^i_8Br^a_x$ and GO-$(TBA)_2Mo_6Br^i_8Br^a_x$, respectively. The quantum yields of methanol by using GO-$Cs_2Mo_6Br^i_8Br^a_x$ and GO-$(TBA)_2Mo_6Br^i_8Br^a_x$ as catalysts with reference to Mo_6 cluster units presented in 0.1 g amount of catalyst were found to be 0.015 and 0.011, respectively. The role of immobilized Mo_6 clusters-based compounds on GO nanosheets is discussed to understand the photocatalytic mechanism of CO_2 reduction into methanol.

1. Introduction

Graphene oxide (GO), an oxidized form of graphene, conventionally served as a most established precursor for the preparation of reduced graphene oxide, chemically functionalized graphene and graphene-based composites [1,2]. Owing to its rich surface chemistry, high specific surface area and various structural defects, GO has attracted large attention not only as a catalytic material, but also as an excellent nanostructured support for heterogenization of various catalysts for efficient chemical transformations [3,4]. The first report on the catalytic activity of GO was revealed by Bielawski et al. in 2010 for the oxidation of various alcohols and the hydration of various alkynes [5]. Then after, the catalytic performance of GO was expanded for various chemical transformations, including oxidation of thiols, sulphides

* *Corresponding author.*
E-mail address: sumanjain@iip.res.in (S.L. Jain).
http://dx.doi.org/10.1016/j.carbon.2015.06.029
0008-6223/

and olefins, aza-Michael addition of amines to activated alkenes, acetalization of aldehydes, ring-opening polymerization of various cyclic lactones and lactams, Friedel–Crafts addition of indoles to α,β-unsaturated ketones, oxidative coupling of amines to imines, oxidative amidation of aromatic aldehydes, etc [6–11]. The catalytic properties of GO are mainly originated from the presence of various oxygen functionalities and unpaired electrons in the GO scaffold and its very high surface area [2,3]. Recently, Riedo et al. have demonstrated that GO is a metastable material, whose structure and chemical functionalities evolve at room temperature [12]. Furthermore, an increase of temperature induces gradual reduction of oxygen functionalities in the GO [13]. The ease of GO aging and reduction during catalytic reactions under mild to high temperature raised the issue of recyclability of GO for chemical transformations [14].

Moreover, the high specific surface area, excellent dispersibility in water/polar solvents, presence of plenty of oxygen containing functional groups and several structural defects in GO scaffold provide ample opportunities to serve as a nano-structured support for heterogenization of catalytically active metal complexes, organic functionalities, and transition metal clusters for efficient chemical transformations [15–19]. In recent years, several methodologies have been established for immobilization of various nano-materials on the GO nanosheets, which include the use of bi-functional linkers, light-induced immobilization, co-reduction of metal salts in the presence of GO, etc [2,20–22]. In most of these approaches, the oxygen functionalities and structural defects in the GO scaffold function as anchoring sites for the immobilization of various types of nanomaterials.

Molybdenum octahedral (Mo_6) clusters with the general formula $A_2Mo_6X^i_8X^a_6$ (A = Cs^+, n-$(C_4H_9)_4N^+$ and X = Br^-) exhibit photochemical and redox properties due to delocalization of valence electrons on the metal centers [23–25]. The Mo_6 clusters are face-capped by eight inner ligands (Br^i) through Mo–Br^i bonds having covalent dominant character, and are additionally bonded to six apical ligands (Br^a) through Mo–Br^a linkage having strong ionic character. The dissolution of these clusters affords $[Mo_6Br^i_8Br^a_6]^{2-}$ anionic units, where the $Mo_6Br^i_8$ core constitutes a rigid block that can be functionalized by exchange/replacement of Br^a located at the apical position of the cluster. Owing to their remarkable structural and photophysical properties, $A_2Mo_6X^i_8X^a_6$ cluster-based compounds provide immense potential for nanoarchitectonic and photocatalytic applications [26]. Recently, Boukherroub et al. have demonstrated that nanocomposites of Mo_6 clusters, gold nanoparticles and GO exhibited very high photocatalytic activity for the degradation of rhodamine B under visible light irradiation. In these photocatalysts, the Mo_6 cluster absorbs the incident photons and initiates the photocatalytic process [24]. The Mo_6 clusters as homogeneous catalyst could also afford photo-reduction of CO_2 into methanol induced by visible light. However, the need of sacrificial donor and non-recyclability of these clusters make the catalytic process expensive [27].

Due to the rising concentration of CO_2 and the depletion of fossil fuel reserves, there is considerable interest in the development of alternative energy sources [28–30]. Conversion of CO_2 into hydrocarbon fuels utilizing the abundant solar energy can provide a viable solution for both problems simultaneously [31,32]. In this regard, a number of heterogeneous catalysts including metal oxides, sulphides, nitrides and oxynitrides have been investigated for CO_2 reduction, albeit lower quantum yields and poor selectivities are the major drawbacks [33–35]. Molecular catalysis, particularly, based on transition metal complexes, such as rhenium (I) bipyridine, ruthenium (II) polypyridine carbonyl, cobalt (II) trisbipyridine, and cobalt (III) macrocycles in combination with a photosensitizer have been considered to be high performance photocatalysts for CO_2 reduction with relatively high quantum yield and high selectivity of products [36–39]. However, the homogeneous nature and non-recycling ability of these catalysts make them impractical from economical as well as environmental viewpoints. This problem can be overcome by anchoring these complexes to photoactive supports, which not only provides facile recovery of the catalyst, but also photoactive support and complex may work synergistically for better electron transfer to CO_2 [40,41]. In a recent report, we have demonstrated the photocatalytic activity of Mo_6 clusters for the photoreduction of CO_2 using triethylamine as the sacrificial agent [27]. However, non-recycling ability of the photocatalyst and need of sacrificial donor (triethylamine) are the major drawbacks of the developed method. Herein, $Cs_2Mo_6Br^i_8Br^a_6$ and $(TBA)_2Mo_6Br^i_8Br^a_6$ clusters are systematically immobilized on GO nanosheets by taking advantage of labile nature of the apical bromide ions and oxygen-functionalities of GO nanosheets. The developed GO-$Cs_2Mo_6Br^i_8Br^a{}_x$ and GO-$(TBA)_2Mo_6Br^i_8Br^a{}_x$ composites (Fig. 1) were then used as heterogeneous photocatalysts for the reduction of CO_2 into methanol.

2. Experimental

2.1. Catalyst preparation

2.1.1. Preparation of GO-$Cs_2Mo_6Br^i_8Br^a{}_x$/GO-$(TBA)_2Mo_6Br^i_8Br^a{}_x$ composite materials

The GO, used as a nanostructured support material for immobilization of Mo_6 clusters, was prepared in two steps using graphite powder as a precursor. Initially, graphite powder was oxidized into graphite oxide using a mixture of H_2SO_4, $NaNO_3$ and $KMnO_4$ as strong oxidants and then the oxidized product was washed with H_2O_2, HNO_3 and ample of water in the subsequent order. In the second step, graphite oxide was exfoliated into GO using ultrasonic probe. The exfoliated product was then centrifuged at 5000 rpm for 15 min to yield two distinct phases: an upper phase containing dispersible fine sheets of GO and a lower deposited semi-solid phase. The fine fraction of GO nanosheets was then used for loading of Mo_6 clusters. The $Cs_2Mo_6Br^i_8Br^a_6$ and $(TBA)_2Mo_6Br^i_8Br^a_6$ cluster-based compounds were synthesized according to a previously reported procedure [42,43]. In brief, initially, Mo_6Br_{12} cluster-based binary bromide was prepared by the reaction of Br_2 with molybdenum powder at 750 °C. Then an excision reaction was performed between a stoichiometric amount of $MoBr_2$ and CsBr at 850 °C for two days. Afterwards, the prepared $Cs_2Mo_6Br^i_8Br^a_6$ was dissolved in dry acetone, filtrated and re-crystallized in pure form. $(TBA)_2Mo_6Br^i_8Br^a_6$ was obtained by precipitation after addition

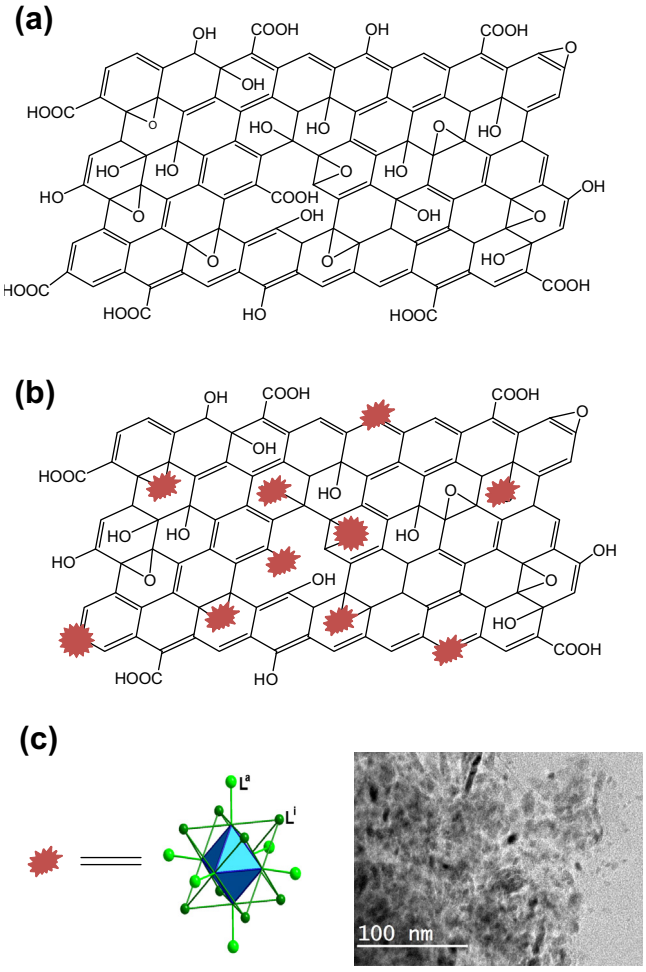

Fig. 1 – A schematic illustration of (a) GO nanosheet decorated with various oxygen functionalities, (b) immobilization of $Cs_2Mo_6Br^i_8Br^a_6$/$(TBA)_2Mo_6Br^i_8Br^a_6$ clusters on the GO nanosheets, and (c) molecular structure of Mo_6 cluster representing position of inner and apical ligands and HRTEM image of GO loaded with ample $Cs_2Mo_6Br^i_8Br^a_6$/$(TBA)_2Mo_6Br^i_8Br^a_6$ clusters. (A color version of this figure can be viewed online.)

of tetrabutyl ammonium bromide in a 50:50 water:ethanol solution of $Cs_2Mo_6Br^i_8Br^a_6$.

In order to immobilize the synthesized Mo_6 clusters on GO nanosheets, 49 mg of $Cs_2Mo_6Br^i_8Br^a_6$ or $(TBA)_2Mo_6Br^i_8Br^a_6$ clusters were separately dispersed in a mixture of water and ethanol (100 and 50 mL, respectively). In the subsequent step, a 50 mL of GO aqueous dispersion (2.24 mg/mL) was gradually added into the dispersion of Mo_6 clusters and the mixture was stirred for 48 h at room temperature. This was followed by filtration of the reaction mixture under vacuum line using membrane filter. During this process, the freely suspended $Cs_2Mo_6Br^i_8Br^a_6$/$(TBA)_2Mo_6Br^i_8Br^a_6$ clusters passed through the membrane. The filtrate cake, composed of immobilized Mo_6 clusters on GO nanosheets was washed five times with ethanol to afford the final product, GO-$Cs_2Mo_6Br^i_8Br^a_x$ or GO-$(TBA)_2Mo_6Br^i_8Br^a_x$. Finally, the product was dried in an oven for chemical and structural characterizations and then used for photocatalytic reduction of CO_2. Fig. 1 shows the schematic illustrations of GO, Mo_6 clusters and immobilized clusters on the GO nanosheets.

2.2. Chemical and structural characterizations of GO-$Cs_2Mo_6Br^i_8Br^a_x$/GO-$(TBA)_2Mo_6Br^i_8Br^a_x$ composite materials

Fourier transform infrared (FTIR) spectra of GO, Mo_6 clusters and their composites were recorded on a Thermo-Nicolet 8700 Research spectrometer (Thermo Scientific) with a resolution of 4 cm^{-1}. X-ray photoelectron spectroscopy (XPS, JPS-9010TRX, JEOL Ltd.) measurements were carried out using thin films of GO, GO-$Cs_2Mo_6Br^i_8Br^a_x$ and GO-$(TBA)_2Mo_6Br^i_8Br^a_x$ samples. The XPS measurements were executed using a MgKα line as the X-ray source. The peak-fitting of the C1s spectra was performed by using a Gaussian–Lorentzian function after performing a Shirley background correction. Thermogravimetric analyses (TGA) were recorded on a thermal analyzer (Diamond, PerkinElmer). All samples were analyzed in the temperature range of 35–550 °C under a steady flow of nitrogen. The high resolution microscopic features of GO, GO-$Cs_2Mo_6Br^i_8Br^a_x$ and GO-$(TBA)_2Mo_6Br^i_8Br^a_x$ samples were examined on high resolution transmission electron microscope (HRTEM) by drop casting their ethanol solutions on the TEM grids. Field emission scanning electron microscopy (FESEM) analyses were carried out using an FEI Quanta 200 F. The elemental distribution in the developed composite materials was recorded by using energy dispersive spectrometer (EDS) coupled with FESEM. UV/Vis spectra were measured on a Hitachi U-2900 UV/Vis spectrometer with a path length of 1 cm using quartz cuvettes.

2.3. Photocatalytic reduction of CO_2

Photocatalytic reduction of CO_2 was carried out using GO-$Cs_2Mo_6Br^i_8Br^a_x$ and GO-$(TBA)_2Mo_6Br^i_8Br^a_x$ composites as the photocatalysts. The experiments were performed in borosil cylindrical vessel (100 mL) of 5 cm diameter. Photo-irradiation was carried out under visible light by using 20 W white cold LED flood light (model No. HP-FL-20 W-F-Hope LED Opto-Electric Co., Ltd.). The intensity of the light at vessel was measured by intensity meter and was found to be 75 Wm^{-2}. The vessel was charged initially with water (10 mL) and DMF (40 mL), and then the solution was degassed by continuous purging of nitrogen for 15 min. Subsequently, CO_2 was bubbled through the solution for at least 30 min to saturate the solution, then GO-$Cs_2Mo_6Br^i_8Br^a_x$ or GO-$(TBA)_2Mo_6Br^i_8Br^a_x$ catalyst (100 mg) was added to the above-described solution. The vessel was tightly closed during the photocatalytic reaction and stirred continuously by a magnetic stirring bar to prevent sedimentation of the catalyst. Samples were collected every 2 h by using a needle, and the catalyst was removed by filtration (0.2 μm PTFE, 13 mm diameter). Quantitative determination of reaction product was achieved by using GC-FID (Varian CP3800 by using CP Sil 24CB LOW BLEED/MS column, flow rate: 0.5 mL min^{-1}, injector temperature: 250 °C, FID detector temperature: 275 °C). A calibration curve was generated for quantification and for confirmation of linear response of the GC-FID system. Further confirmation of methanol production was done by HPLC (Shimadzu UFLC, by using Oyster BDS Premium C18 250X4.6 mm, 5 μm column, mobile phase acetonitrile:acetone

(65:35), flow rate: 0.5 mL/min at 205 nm). Blank reactions were conducted to ensure that methanol production was due to the photo-reduction of CO_2 and to eliminate surrounding interference. For the determination of gaseous products, 20 μL sample was withdrawn and analyzed with the help of GC-TCD and GC-FID (Agilent 7890A GC system) equipped with RGA (refinery gas analyzer) capillary column; flow rate (H_2: 35 mL/min, air: 350 mL/min, makeup flow: 27 mL/min, for TCD reference flow: 45 mL/min, Helium flow: 2 mL/min), injector temperature: 220 °C, TCD detector temperature and FID detector temperature: 220 °C.

3. Results and discussion

3.1. *Synthesis and characterization of catalyst*

The chemical and structural features of GO and its composites i.e., GO-$Cs_2Mo_6Br^i_8Br^a_x$ and GO-$(TBA)_2Mo_6Br^i_8Br^a_x$ were thoroughly characterized by FTIR, XPS, TG-DTA, HRTEM, EDX and UV–Vis analyses. The FTIR spectrum of GO (Fig. 2) exhibited strong characteristics vibrational bands at 3419, 1732, 1622, 1373, 1263 and 1064 cm^{-1}, which are attributed to O–H stretch, C=O stretch, H_2O bending modes and C=C stretch, O–H bending and C–O stretch, respectively. The strong intensities of these vibrations revealed the presence of ample hydroxyl, epoxy, carboxylic, carbonyl, phenolic, etc. functional groups in the GO scaffold. The $Cs_2Mo_6Br^i_8Br^a_x$ has no vibrational signature, except a strong band at 1620 cm^{-1}, attributed to the bending mode of adsorbed water molecules in the cluster compound (Fig. 2a).

In contrast, $(TBA)_2Mo_6Br^i_8Br^a_6$ showed strong characteristic vibrational modes in the range of 3000–2800 cm^{-1}, attributed to the C–H stretches of methylene and methyl groups (Fig. 2b). Furthermore, strong vibrations at 1466 and 1383 cm^{-1} associated with C–H bending modes revealed the presence of butyl chains in the $(TBA)_2Mo_6Br^i_8Br^a_6$ clusters. The appearance of C–H vibrations in the GO-$(TBA)_2Mo_6Br^i_8Br_x{}^a$ composite (inset of Fig. 2b) suggested the loading of $(TBA)_2Mo_6Br^i_8Br^a_6$ on the GO nanosheets. Both GO-$Cs_2Mo_6Br^i_8Br^a_x$ and GO-$(TBA)_2Mo_6Br^i_8Br^a_x$ composites exhibited the characteristic vibrations of oxygen functionalities of GO, indicating that most of oxygen functionalities were remained intact and presented in both GO-$Cs_2Mo_6Br^i_8Br^a_x$ and GO-$(TBA)_2Mo_6Br^i_8Br^a_x$ composites. In order to probe the chemical states and plausible interaction between the Mo_6 clusters and GO, all samples were thoroughly characterized by XPS.

XPS analyses of GO, GO-$Cs_2Mo_6Br^i_8Br^a_x$ and GO-$(TBA)_2Mo_6Br^i_8Br^a_x$ samples were carried out to elucidate the quantitative estimation along with chemical changes in the GO and Mo_6 clusters (Figs. 3 and 4). The high-resolution C 1s spectrum of GO exhibited an overlapped double peak structure with small tail at higher binding energy attributed to different types of oxygen containing functional groups in the GO scaffold. The peak-fitting of C 1s spectrum of GO can be deconvoluted into five chemically-shifted components (Fig. 3a). The C 1s peak centered at 284.9 eV as a major component of GO scaffold is attributed to C–C/C–H carbons. The peak at relatively lower binding energy (284.0 eV) is due to C=C carbon and suggests the presence of unoxidized domains of sp^2 carbon. Three

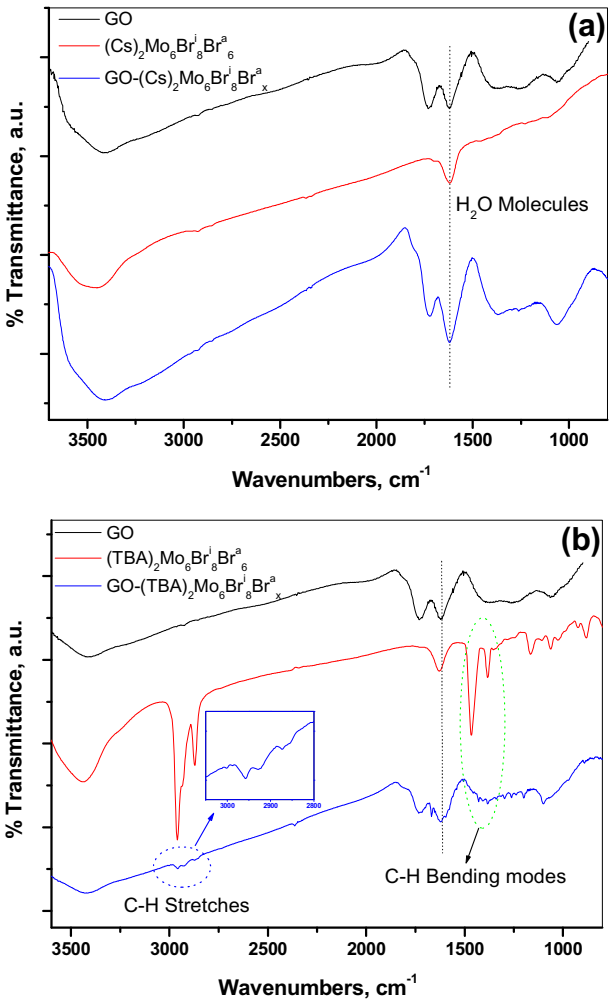

Fig. 2 – FTIR spectra of (a) GO, $Cs_2Mo_6Br^i_8Br^a_6$ clusters and GO-$Cs_2Mo_6Br^i_8Br^a_x$ composite, and (b) GO, $(TBA)_2Mo_6Br^i_8Br^a_6$ clusters and GO-$(TBA)_2Mo_6Br^i_8Br^a_6$ composite. The presence of C–H vibrational modes in GO-$(TBA)_2Mo_6Br^i_8Br^a_x$ composite reveals the loading of $(TBA)_2Mo_6Br^i_8Br^a_6$ clusters on the GO nanosheets. (A color version of this figure can be viewed online.)

additional overlapped components at 286.8, 288.6 and 289.5 eV are assigned to the hydroxyl/epoxide (C–OH/C–O–C), carbonyl (C=O) and carboxyl (COOH) functional groups, respectively [44,45]. Fig. 3 indicates that all characteristic peaks of C 1s spectra remained intact, when Mo_6 clusters were immobilized on the GO nanosheets and no significant changes were observed. Furthermore, the loading of Mo_6 clusters onto GO nanosheets was deduced by appearance of additional peaks at 724.5, 229.3 and 70.2 eV attributed to Cs 3d, Mo 3d and Br 3d, respectively (Fig. 4). The Mo 3d peaks at 229.3 and 232.4 eV are due to the split components of $3d_{5/2}$ and $3d_{3/2}$, respectively and revealed the Mo(II) oxidation state [24,46]. The positions of Mo $3d_{5/2}$ and $3d_{3/2}$ components in the GO-$Cs_2Mo_6Br^i_8Br^a_x$ and GO-$(TBA)_2Mo_6Br^i_8Br^a_x$ are comparable to those obtained for their pure Mo_6 clusters. These results suggest that the cluster core $Mo_6Br^i_8$ remained intact during cluster immobilization on the GO nanosheets. The Cs 3d peaks at 724.5 and 739 eV

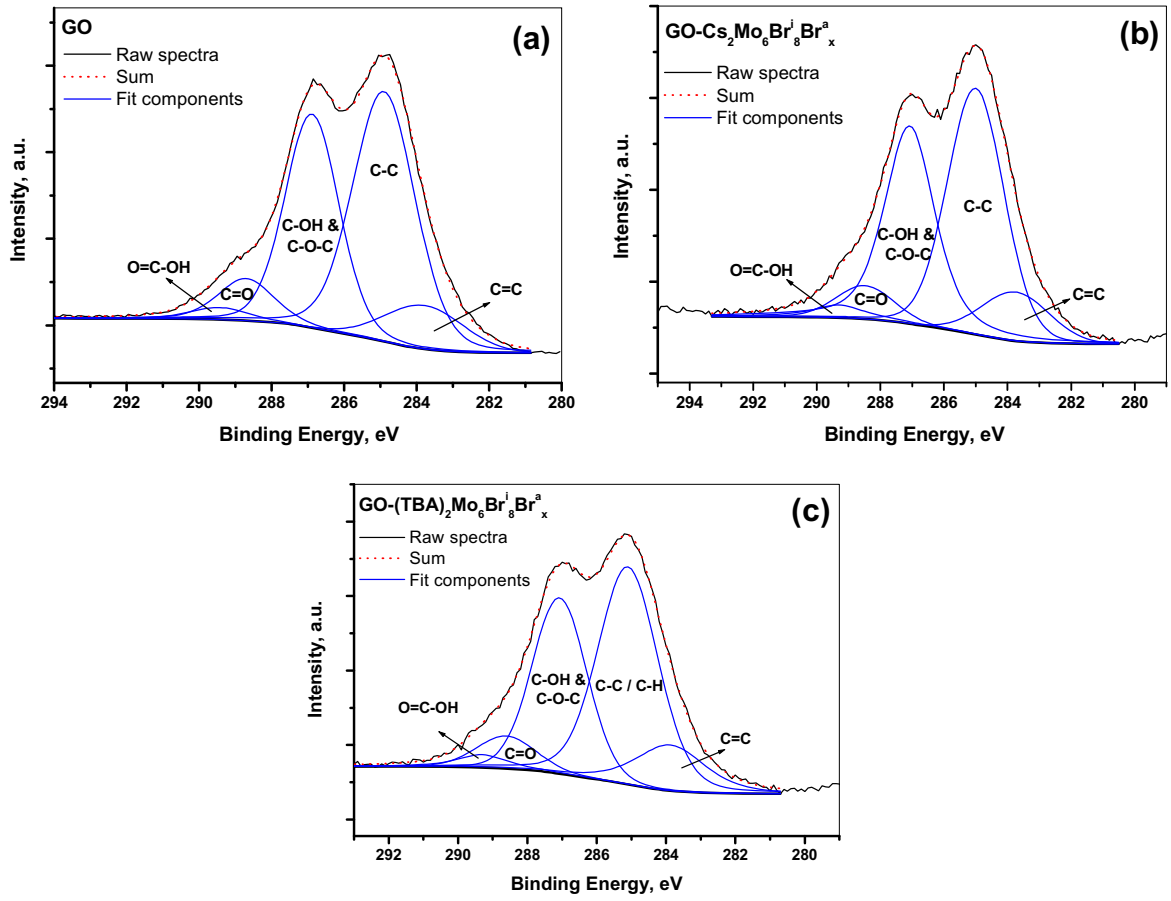

Fig. 3 – High resolution C 1s XPS spectra of (a) GO, (b) GO-$Cs_2Mo_6Br^i_8Br^a_x$ and (c) GO-$(TBA)_2Mo_6Br^i_8Br^a_x$ samples. The deconvoluted components illustrate the various types of oxygen functionalities in the materials. (A color version of this figure can be viewed online.)

are attributed to the split components of $3d_{5/2}$ and $3d_{3/2}$, respectively and indicate the presence of Cs(I) in the GO-$Cs_2Mo_6Br^i_8Br^a_x$ composite (Fig. 4a). The Cs $3d_{3/2}$ peak could not appear explicitly, as it was diminished by nearby strong peak of O (KVV) as shown in Fig. S1 (Electronic Supporting Information).

The internal core of the octahedral Mo_6 clusters consists of eight Mo–Br^i bonds and the remaining six Br^- are placed on apical position through Mo–Br^a bonds having strong ionic character. These apical Br^- functionalities are prone to interact with other chemical functionalities and facilitate their immobilization onto solid supports. The XPS spectra of Mo_6 cluster compounds and their immobilized composites GO-$Cs_2Mo_6Br^i_8Br^a_x$ and GO-$(TBA)_2Mo_6Br^i_8Br^a_x$ are shown in Fig. 4c and d. The Br 3d peak in Mo_6 clusters is composed of two components at 70.2 and 68.6 eV, which are attributed to covalently bonded inner Br atoms (Br^i) and apical bromide ions (Br^a) of Mo_6 clusters, respectively [47,48]. The Br 3d spectra of GO-$Cs_2Mo_6Br^i_8Br^a_x$ and GO-$(TBA)_2Mo_6Br^i_8Br^a_x$ composites (Fig. 4c and d) showed that the peak component at 68.6 eV, attributed to Br^a ligands, is almost diminished, demonstrating the elimination of Br^a ligands. This suggests the reaction of Br^a of Mo_6 clusters with hydroxyl/oxygen carrying functional groups of GO nanosheets. As a result, Mo_6 clusters immobilized on the GO nanosheets by covalent linkage and Br^a are eliminated during immobilization process. The atomic % of Mo and Br components in both $(TBA)_2Mo_6Br^i_8Br^a_6$ cluster and GO-$(TBA)_2Mo_6Br^i_8Br^a_x$ composites were calculated based on XPS study, to determine the interaction between the $(TBA)_2Mo_6Br^i_8Br^a_6$ cluster and GO nanosheets. The experimental ratio of Br/Mo = 2.6 in $(TBA)_2Mo_6Br^i_8Br^a_6$ cluster agrees with the theoretical value (2.33). After immobilization of $(TBA)_2Mo_6Br^i_8Br^a_6$ cluster, the ratio of Br/Mo decreased to 1.6, which is closer to the expected value (1.33) for a Br^i/Mo cluster core. Recently, Sutherland et al. have further demonstrated that labile terminal nitro groups at apical position in Mo_6 clusters were eliminated during their chemical attachment to solid supports [49].

UV/Vis absorption spectra of $Cs_2Mo_6Br^i_8Br^a_6$ and $(TBA)_2Mo_6Br^i_8Br^a_6$ in acetonitrile exhibited sharp peaks at 242 and 243 nm due to the inter ligand transition and small humps at 386 and 380 nm due to the metal-to-ligand charge-transfer (MLCT) transitions, respectively (Fig. S2a and b). For GO, a characteristic absorption band at 227 nm due to $\pi \rightarrow \pi^*$ transition of discrete units of sp^2 carbon conjugated network and a small hump at 300 nm due to $n \rightarrow \pi^*$ of carbonyl groups were observed. Immobilization of Mo_6 clusters to GO enhanced the overall absorption pattern as shown in Fig. S2.

In order to confirm the visible light absorption, we calculated the band gap of GO, $Cs_2Mo_6Br^i_8Br^a_6$ cluster, GO-$Cs_2Mo_6Br^i_8Br^a_x$ composite, $(TBA)_2Mo_6$ $Br^i_8Br^a_6$ cluster and

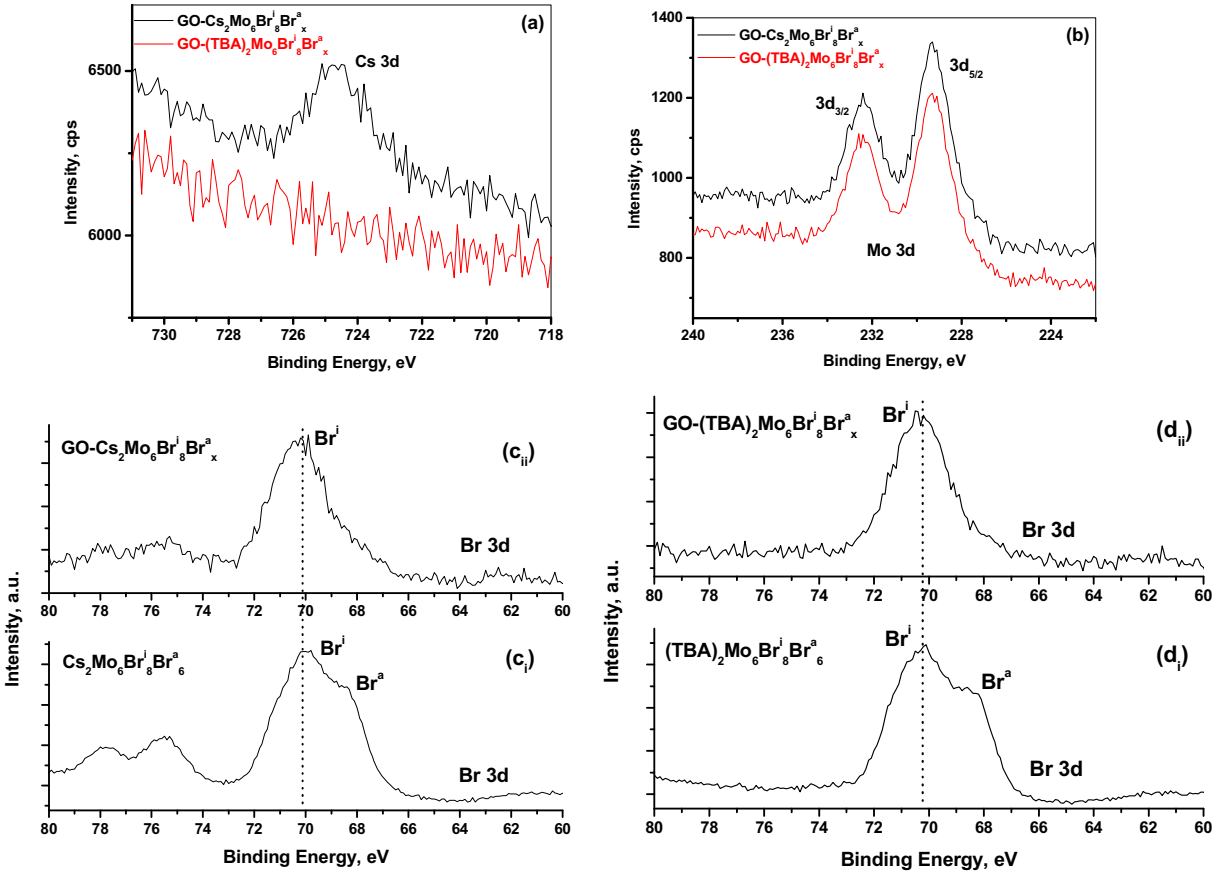

Fig. 4 – XPS spectra of (a) Cs 3d; (b) Mo 3d regions for GO-$Cs_2Mo_6Br^i_8Br^a_x$ and GO-$(TBA)_2Mo_6Br^i_8Br^a_x$; (c) Br 3d region for $Cs_2Mo_6Br^i_8Br^a_6$ and GO-$Cs_2Mo_6Br^i_8Br^a_x$ (d) Br 3d regions for $(TBA)_2Mo_6Br^i_8Br^a_6$ and GO-$(TBA)_2Mo_6Br^i_8Br^a_x$ composites. (A color version of this figure can be viewed online.)

GO-$(TBA)_2Mo_6$ $Br^i_8Br^a_x$ composite with the help of Tauc plot as shown in Fig. S3. The band gap value for GO was found to be 2.90 eV was in well agreement with the reported literature [50]. For $Cs_2Mo_6Br^i_8Br^a_6$ and $(TBA)_2Mo_6Br^i_8Br^a_6$ clusters compounds, two band gap values were obtained; the 4.07 and 4.16 eV were due to the interligand transitions while the 2.40 and 2.47 eV were ascribed to the MLCT transitions, respectively. After immobilization of Mo_6 clusters on GO, the band gap values significantly decreased to 0.9 and 1.5 eV for GO-$Cs_2Mo_6Br^i_8Br^a_x$ and GO-$(TBA)_2Mo_6Br^i_8Br^a_x$ composite, respectively.

The thermal behavior of GO, Mo_6 clusters and their composites were examined by thermogravimetric analysis (TGA). GO showed two characteristic major weight losses in the range of 50–110 °C and 170–240 °C, owing to evaporation of trapped water molecules and thermal decomposition of labile oxygen functionalities in GO scaffold, respectively (Fig. 5). The $Cs_2Mo_6Br^i_8Br^a_6$ cluster is found to be thermally stable up to 500 °C, whereas $(TBA)_2Mo_6Br^i_8Br^a_6$ cluster has significant mass loss about 27% in the range of 320–390 °C with maximum loss at 368 °C, most likely due to the thermal decomposition of TBA units (Fig. 5b_{ii}). However, GO-$(TBA)_2Mo_6Br^i_8Br^a_x$ composite showed 4.5% weight loss (due to TBA units and oxygen functionalities of GO) in the range of 295–375 °C with maximum loss at 340 °C (Fig. 5b_{iii}). Plausibly, the presence of residual oxygen functionalities in the GO-$(TBA)_2Mo_6Br^i_8Br^a_x$ composite has facilitated the decomposition of TBA units in supported composite comparatively at lower temperature. Based on the TGA results, the calculated weight loss due to the supported TBA cluster units was found to be 1.6%.

The nano-structural features of GO and its composites with Mo_6 clusters were examined by HRTEM. Fig. 6a shows plenty of wrinkle and folded regions in the HRTEM image of GO scaffolds. These features are attributed to the sp^3 carbons, which are linked to oxygen functionalities in the basal plane and various structural defects. Significant structural changes are observed when Mo_6 clusters were immobilized on GO nanosheets (Fig. 6b and c). The Mo_6 clusters are uniformly distributed over the GO surface and they are seen as dark gray features in the range of 2–10 nm. The hydrodynamic diameter of $Cs_2Mo_6Br^i_8Br^a_6$ clusters is reported to be 2.5 nm by dynamic light scattering (DLS) method, whereas the crystallographic cluster unit size of these clusters is 1.1 nm [25]. The larger size of immobilized Mo_6 clusters on GO nanosheets along with their undefined structure suggest that the Mo_6 clusters are immobilized on the GO not only as single unit of each cluster, but also in form of aggregates composed of 2–7 units. Usually, these Mo_6 clusters agglomerate because of the electrostatic attraction between anionic parts of one cluster unit and counter cationic part of another unit. Furthermore, elemental mapping of GO-$Cs_2Mo_6Br^i_8Br^a_x$ and GO-$(TBA)_2Mo_6Br^i_8Br^a_x$ composites based on EDS measurements was carried out to reveal

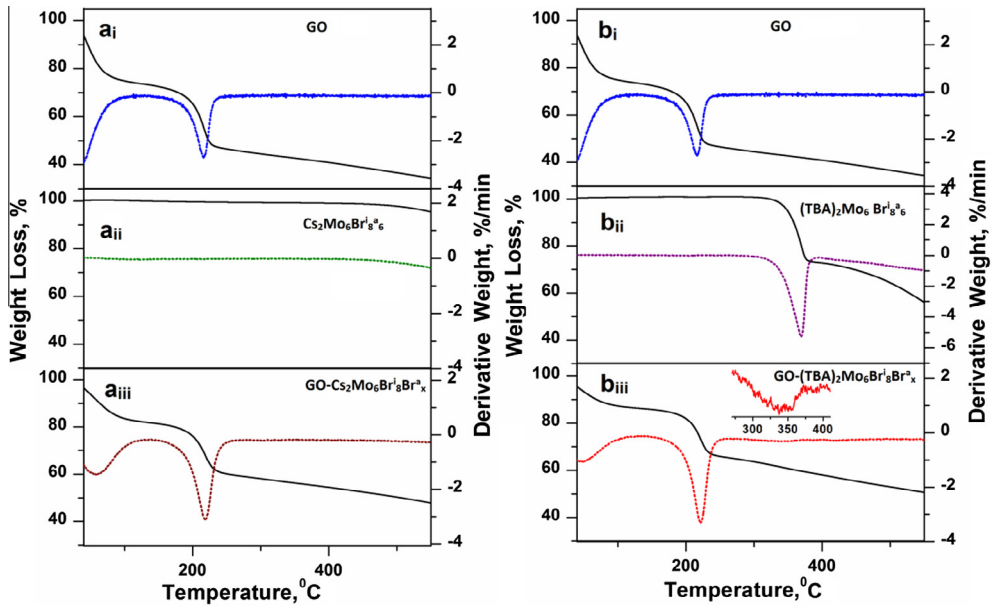

Fig. 5 – TG-DTA patterns of (a) GO, $Cs_2Mo_6Br^i_8Br^a_6$ cluster and GO-$Cs_2Mo_6Br^i_8Br^a_x$ composite; (b) GO, $(TBA)_2Mo_6Br^i_8Br^a_6$ cluster and GO-$(TBA)_2Mo_6Br^i_8Br^a_x$ composite over the temperature range of 30–550 °C under nitrogen flow. (A color version of this figure can be viewed online.)

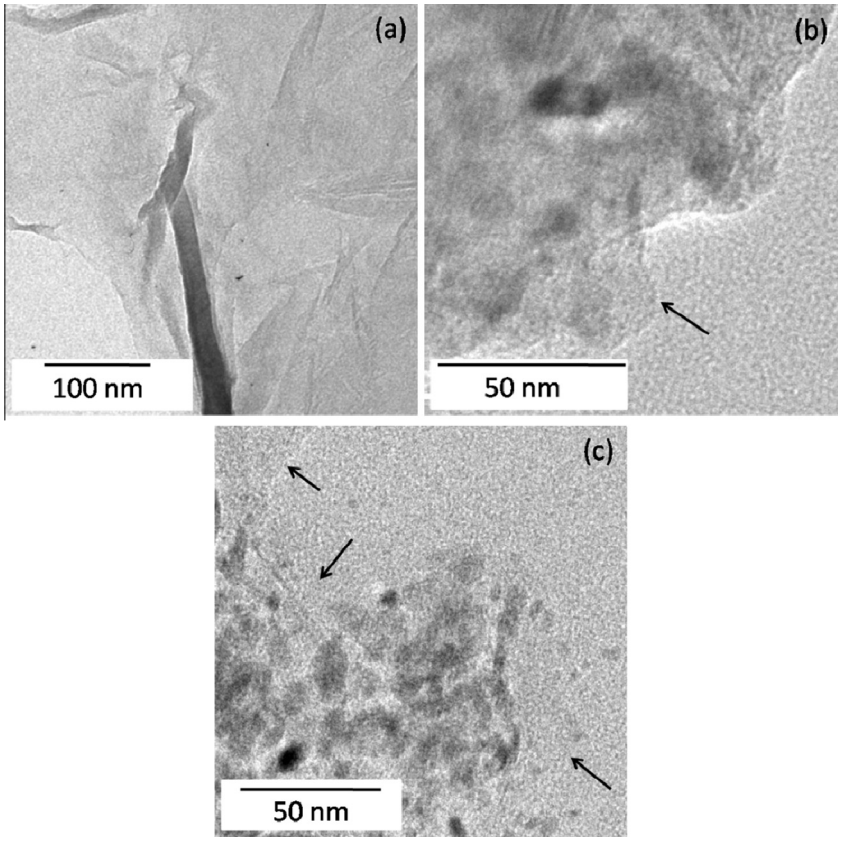

Fig. 6 – HRTEM images of (a) GO nanosheets. Distribution of hexamolybdenum clusters on GO nanosheets: (b) GO-$Cs_2Mo_6Br^i_8Br^a_x$ and (c) GO-$(TBA)_2Mo_6Br^i_8Br^a_x$ composites.

the distribution of Mo_6 clusters on the GO nanosheets. Fig. S4 (Supporting Information) shows FESEM micrographs and the corresponding elemental mapping of GO-$Cs_2Mo_6Br^i_8Br^a_x$ and GO-$(TBA)_2Mo_6Br^i_8Br^a_x$ composites. The thorough and uniform distribution of cesium, molybdenum and bromide as characteristic elements in GO-$Cs_2Mo_6Br^i_8Br^a_x$ composite and

nitrogen, molybdenum and bromide in GO-$(TBA)_2Mo_6Br^i_8Br^a_x$ composite indicate that Mo_6 clusters are uniformly immobilized on GO nanosheets, which is very important for efficient photocatalytic activities of developed composite materials. The molybdenum content in the GO-$Cs_2Mo_6Br^i_8Br^a_x$ and GO-$(TBA)_2Mo_6Br^i_8Br^a_x$ composites was found to be 0.74 and 0.73 atomic %, respectively, as determined by XPS analysis.

3.2. *Photocatalytic reduction of CO_2*

The photocatalytic activity of the synthesized GO-$Cs_2Mo_6Br^i_8Br^a_x$ and GO-$(TBA)_2Mo_6Br^i_8Br^a_x$ composite materials for CO_2 reduction was examined in water/DMF mixture under visible light irradiation by using 20 watt white cold LED flood light. During the photoreduction, 0.5 mL reaction mixture was withdrawn gradually. Then 1 μL withdrawn reaction mixture was injected in a GC-FID system for quantitative estimation. The performance of the catalysts was evaluated in term of methanol (MeOH) yield as it was the only liquid reduction product. The MeOH yield (μmol g^{-1} cat) with respect to time using $Cs_2Mo_6Br^i_8Br^a_6$, $(TBA)_2Mo_6Br^i_8Br^a_6$, GO-$Cs_2Mo_6Br^i_8Br^a_x$ and GO-$(TBA)_2Mo_6Br^i_8Br^a_x$ composite as catalyst is displayed in Fig. 7. Both GO-$Cs_2Mo_6Br^i_8Br^a_x$ and GO-$(TBA)_2Mo_6Br^i_8Br^a_x$ exhibited higher photocatalytic activity as compared to GO and Mo_6 clusters. Furthermore, among the two catalysts studied, GO-$Cs_2Mo_6Br^i_8Br^a_x$ was found to be superior than GO-$(TBA)_2Mo_6Br^i_8Br^a_x$. After 24 h illumination, the yield of methanol using GO-$Cs_2Mo_6Br^i_8Br^a_x$, GO-$(TBA)_2Mo_6Br^i_8Br^a_x$, GO, $Cs_2Mo_6Br^i_8Br^a_6$, and $(TBA)_2Mo_6Br^i_8Br^a_6$ as catalysts under identical experimental conditions was found to be 1644, 1294, 439, 285 and 238, μmol g^{-1} cat, respectively with the corresponding methanol formation rate (R_{MeOH}) of 68.5, 53.9, 18.2, 11.8 and 9.9 μmol g^{-1} cat h^{-1}, respectively. The turnover number (TON) and quantum yield for $Cs_2Mo_6Br^i_8Br^a_6$ cluster were found to be 3.30 and 0.0026, respectively, whereas, for $(TBA)_2Mo_6Br^i_8Br^a_6$ cluster the values were 2.75 and 0.0021, respectively. The TON by using GO-$Cs_2Mo_6Br^i_8Br^a_x$ and GO-$(TBA)_2Mo_6Br^i_8Br^a_x$ was found to be 19.0, and 10.38, respectively with respect to Mo_6 cluster and the quantum yields of methanol with reference to Mo_6 cluster units presented in 0.1 g amount of catalyst were found to be 0.015 and 0.011, respectively. The TON of methanol per mole of graphene oxide was calculated by considering the equivalent formula of GO as $C_6(O)$, which was found to be 0.04. The formation of methanol was further confirmed by HPLC analysis as depicted in Figs. S5 and S6. For the quantitative estimation of methanol, a calibration curve was plotted by injecting an exact amount of methanol (1 μL) in GC-FID (Fig. S8). Then the concentration of methanol produced by photo-induced CO_2 reduction was calculated by injecting 1.0 μL of the final reaction solution in GC-FID and comparing the peak area with calibration curve for methanol standard. Further HPLC analysis was performed to confirm the formation of methanol as the only liquid product obtained from the photoreduction of CO_2. Gaseous reaction products were analyzed by GC-FID and GC-TCD and confirmed that there was no gaseous product such as H_2, CO, CH_4 formed during the photoreduction of CO_2. As methanol was obtained as the only product from CO_2 photoreduction under the described experimental conditions, so the catalytic selectivity (CS) of GO-Mo_6 clusters was 100%.

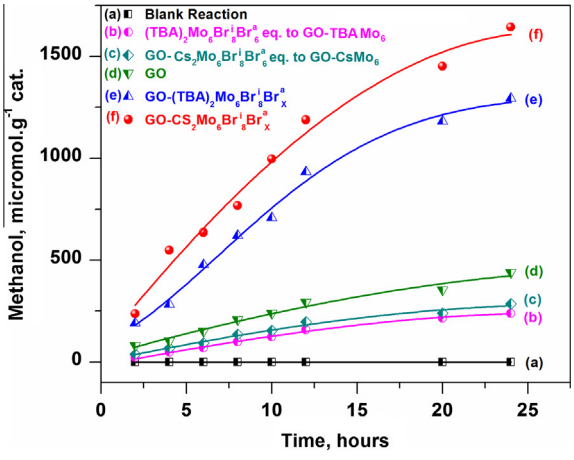

Fig. 7 – Methanol formation rate in (a) blank reaction, (b and c) using $(TBA)_2Mo_6Br^i_8Br^a_6$ and $Cs_2Mo_6Br^i_8Br^a_6$ in equimolar amounts as presented in GO-composites, (d) GO, (e) GO-$(TBA)_2Mo_6Br^i_8Br^a_x$ and (f) GO-$Cs_2Mo_6Br^i_8Br^a_x$ catalyzed photoreduction of CO_2. (A color version of this figure can be viewed online.)

Blank experiments were conducted to ensure that the product formed was due to CO_2 photoreduction. The blank tests consisted of visible light irradiation in the absence of catalyst (Table 1, entry 1) and reaction in the dark with the catalyst (Table 1, entry 2) under otherwise identical experimental conditions. An additional blank test was performed by illuminating the reaction mixture in the presence of photocatalyst by filling N_2 rather than CO_2 (Table 1, entry 3). In all cases, no organic product was obtained even after 24 h visible light exposure.

Last but not least, we established the recycling of the developed heterogeneous cluster catalysts. The results of these recycling experiments are exhibited in Fig. 8. As shown, both heterogeneous GO-Mo photocatalysts exhibited efficient recycling for runs and provided almost similar yield of methanol under identical experimental conditions. These studies suggested that the developed catalysts were highly stable and the reaction was truly heterogeneous in nature.

A plausible mechanism for the CO_2 photoreduction to methanol using GO immobilized Mo_6 clusters as catalysts on the basis of their band gap is illustrated in Fig. 9. The presence of oxygen containing functionalities on GO transforms aromatic sp^2 carbons into sp^3 carbons and creates a network of enormous sp^2 (conduction band) and sp^3 carbon domains (valence band) on GO sheet. Due to presence of several conductive sp^2 carbon domains and non conductive sp^3 carbon containing domains on GO sheet, a band gap is created and it works like a semiconductor [51–53]. The band gap for GO was found to be 2.9 eV in good agreement with the literature values of 2.9–3.7 eV as reported by Hsu et al. [50]. On the other hand, Mo_6 clusters due to their lower band gap values have good visible light absorbance; hence to improve the performance of GO in visible light, Mo_6 clusters were immobilized on the surface of GO via replacement of labile bromine atoms. After absorption of visible light, Mo_6 cluster was transformed to excited state Mo^*_6 by HOMO to LUMO transition and the

Table 1 – Photocatalytic reduction of CO_2 into methanol under controlled experimental conditions.

Entry	Catalyst	React. precursor	Visible light illumination	T (h)	TON
1	Nil	CO_2	Yes	24	–
2	GO-$Cs_2Mo_6Br^i_8Br^a_x$	CO_2	No	24	–
3	GO-$Cs_2Mo_6Br^i_8Br^a_x$	N_2	Yes	24	–
4	$Cs_2Mo_6Br^i_8Br^a_6$	CO_2	Yes	24	3.30
5	$(TBA)_2Mo_6Br^i_8Br^a_6$	CO_2	Yes	24	2.75
4	GO	CO_2	Yes	24	0.04
5	GO-$Cs_2Mo_6Br^i_8Br^a_x$	CO_2	Yes	24	19.0
6	GO-$(TBA)_2Mo_6Br^i_8Br^a_x$	CO_2	Yes	24	10.38

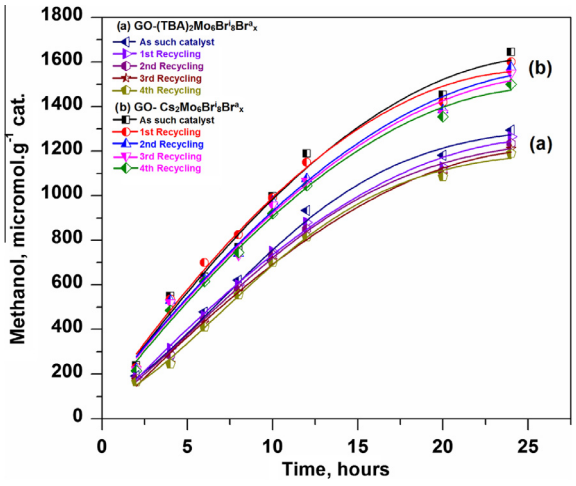

Fig. 8 – Recycling experiments using (a) GO-$(TBA)_2Mo_6Br^i_8Br^a_x$ and (b) GO-$Cs_2Mo_6Br^i_8Br^a_x$. (A color version of this figure can be viewed online.)

excited Mo_6^* transfers electron to the conduction band of GO (Fig. 9). These electrons in the conduction band of GO were used for the reduction of CO_2 to give methanol [54–56]. The positively charged Mo_6^+ cluster gets electron from valence band of GO and transforms back into its original (Mo_6) state. Water splitting at the valance band of GO possibly provides necessary electrons and protons for the reduction of CO_2 to methanol. Furthermore, due to the better charge mobility and higher surface area, GO improves the catalytic performance synergistically [57–59].

$$6Mo_6 \text{ cluster} + h\nu \rightarrow 6Mo_6^* \text{ cluster(excited state)}$$

$$6Mo_6^* \text{ cluster(excited state)} + GO \rightarrow 6e^- \text{(GO conduction band)} + 6Mo_6^+ \text{ cluster}$$

$$6e^- \text{(GO conduction band)} + CO_2 + 6H^+ \rightarrow CH_3OH + H_2O$$

$$3H_2O \rightarrow 6H^+ + 6e^- + 3/2O_2$$

$$6Mo_6^+ \text{ cluster} + 6e^- \rightarrow 6Mo_6 \text{ cluster}$$

$$\text{Overall reaction } CO_2 + 6H^+ + 6e^- \rightarrow CH_3OH + H_2O$$

4. Conclusion

Hexamolybdenum cluster compounds i.e., $Cs_2Mo_6Br^i_8Br^a_6$ and $(TBA)_2Mo_6Br^i_8Br^a_6$ were immobilized on GO nanosheets and the resulting composites were used for the photocatalytic reduction of CO_2 to methanol under visible light irradiation without adding any sacrificial agent. Owing to the wide band gap, GO alone does not provide excitation in the visible. The Mo_6 units located on the surface of GO act as visible light absorbers and facilitate the transfer of electrons to GO

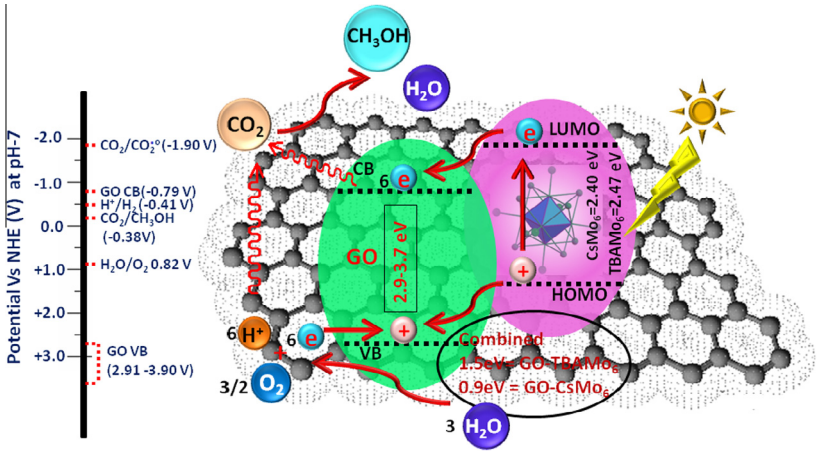

Fig. 9 – Plausible mechanism of photoreduction of CO_2 into methanol catalyzed by GO-hexamolybdenum composite. (A color version of this figure can be viewed online.)

conduction band. After 24 h of visible light illumination, the yield of methanol was found to be 1644 and 1294 μmol g^{-1} cat for GO-$Cs_2Mo_6Br^i_8Br^a_x$ and GO-$(TBA)_2Mo_6Br^i_8Br^a_x$, respectively. These values are much higher than GO alone (439 μmol g^{-1}-cat). However, the facile recovery, efficient recycling and no need of sacrificial donors such as triethylamine make the developed methodology superior and more advantageous for converting CO_2 to high value chemicals.

Acknowledgements

We kindly acknowledge Director, CSIR-IIP for his permission to publish these results. P.K. and H.P.M. are thankful to CSIR and UGC, New Delhi, respectively for providing research fellowship. Analytical department of the Institute is kindly acknowledged for providing support in analysis. DST, New Delhi is kindly acknowledged for providing financial support.

Appendix A. Supplementary data

Supplementary data associated with this article can be found, in the online version, at http://dx.doi.org/10.1016/j.carbon.2015.06.029.

REFERENCES

[1] Dreyer DR, Park S, Bielawski CW, Ruoff RS. Chem Soc Rev 2010;39:228–40.
[2] Georgakilas V, Otyepka M, Bourlinos AB, Chandra V, Kim N, Kemp KC, et al. Chem Rev 2012;112:6156–214.
[3] Navalon S, Dhakshinamoorthy A, Alvaro M, Garcia H. Chem Rev 2014;114:6179–212.
[4] Dreyer DR, Todd AD, Bielawski CW. Chem Soc Rev 2014;43:5288–301.
[5] Dreyer DR, Jia HP, Bielawski CW. Angew Chem Int Ed 2010;49:6813–6.
[6] Jia HP, Dreyer DR, Bielawski CW. Adv Synth Catal 2011;353:528–32.
[7] Dreyer DR, Jia HP, Todd AD, Geng J, Bielawski CW. Org Biomol Chem 2011;9:7292–5.
[8] Verma S, Mungse HP, Kumar N, Choudhary S, Jain SL, Sain B, et al. Chem Commun 2011;47:12673–5.
[9] Dhakshinamoorthy A, Alvaro M, Puche M, Fornes V, Garcia H. Chem Catal Chem 2012;4:2026–30.
[10] Dreyer DR, Jarvis KA, Ferreira JP, Bielawski CW. Polym Chem 2012;3:757–66.
[11] Su C, Acik M, Takai K, Lu J, Hao S, Zheng Y, et al. Nat Commun 2012;3:1298.
[12] Kim S, Zhou S, Hu Y, Acik M, Chabal YJ, Berger C, et al. Nat Mater 2012;11:544–9.
[13] Choudhary S, Mungse HP, Khatri OP. Chem Asian J 2013;8:2070–8.
[14] Mungse HP, Bhakuni N, Tripathi D, Sharma OP, Sain B, Khatri OP. J Phys Org Chem 2014;27:944–51.
[15] Li Y, Gao W, Ci L, Wang C, Ajayan PM. Carbon 2010;48:1124–30.
[16] Scheuermann GM, Rumi L, Steurer P, Bannwarth W, Mulhaupt R. J Am Chem Soc 2009;131:8262–70.
[17] Huang J, Zhang L, Chen B, Ji N, Chen F, Zhang Y, et al. Nanoscale 2010;2:2733–8.
[18] Mungse HP, Verma S, Kumar N, Sain B, Khatri OP. J Mater Chem 2012;22:5427–33.
[19] Yuan C, Chen W, Yan L. J Mater Chem 2012;22:7456–60.
[20] Kamat PV. J Phys Chem Lett 2010;1:520–7.
[21] Moon G, Kim H, Shin Y, Choi W. RSC Adv 2012;2:2205–7.
[22] Williams G, Kamat PV. Langmuir 2009;25:13869–73.
[23] Maverick AW, Najdzionek JS, Mackenzie D, Nocera DG, Gray HB. J Am Chem Soc 1983;105:1878–82.
[24] Barras A, Das MR, Devarapalli RR, Shelke MV, Cordier S, Szunerits S, et al. Appl Catal B 2013;130–131:270–6.
[25] Grasset F, Dorson F, Cordier S, Molard Y, Perrin C, Marie AM, et al. Adv Mater 2008;20:143–8.
[26] Cordier S, Grasset F, Molard Y, Amela-Cortes M, Boukherroub R, Ravaine S, et al. J Inorg Organomet Polym Mater 2015;25:189–204.
[27] Kumar P, Kumar S, Cordier S, Paofai S, Boukherroub R, Jain SL. RSC Adv 2014;4:10420–3.
[28] Olah GA. Angew Chem Int Ed 2013;52:104–7.
[29] Aresta M. In: Tolman WB, editor. Carbon dioxide reduction and use as a chemical feedstock. Weinheim, Germany: Wiley-VCH; 2006. p. 1–41.
[30] Indrakanti VP, Kubicki JD, Schobert HH. Energy Environ Sci 2009;2:745–58.
[31] Tran PD, Wong LH, Barber J, Loo JSC. Energy Environ Sci 2012;5:5902.
[32] Halmann MM, Steinberg M. Greenhouse gas carbon dioxide mitigation science and technology. Boca Raton, Florida: Lewis Publishers; 1999.
[33] Izumi Y. Coord Chem Rev 2013;257:171–86.
[34] Habisreutinger SN, Mende LS, Stolarczyk JK. Angew Chem Int Ed 2013;52:7372–408.
[35] Cowan AJ, Durrant JR. Chem Soc Rev 2013;42:2281–93.
[36] Morris AJ, Meyer GJ, Fujita E. Acc Chem Res 2009;42:1983–94.
[37] Inagakia A, Akita M. Coord Chem Rev 2010;254:1220–39.
[38] Reithmeier R, Bruckmeier C, Rieger B. Catalysts 2012;2:544–71.
[39] Takeda H, Ishitani O. Coord Chem Rev 2010;254:346–54.
[40] Zhou XT, Ji HB, Huang XJ. Molecules 2012;17:1149–58.
[41] Ragoussi ME, Malig J, Katsukis G, Butz B, Spiecker E, Torre de la G, et al. Angew Chem Int Ed 2012;51:6421–5.
[42] Kirakci K, Cordier S, Perrin C. Z Anorg Allg Chem 2005;631:411–6.
[43] Schaefer H, Schnering HG, Tillack J, Kuhnen F, Woehrle H, Baumann H, et al. Allg Chem 1967;353:281–310.
[44] Yang D, Velamakanni A, Bozoklu G, Park S, Stoller M, Piner R, et al. Carbon 2009;47:145–52.
[45] Akhavan O. ACS Nano 2010;4:4174–80.
[46] Ababou-Girard S, Cordier S, Fabre B, Molard Y, Perrin C. ChemPhysChem 2007;8:2086–90.
[47] Aubert T, Cabello-Hurtado F, Esnault M-A, Neaime C, Lebret-Chauvel D, Jeanne S, et al. J Phys Chem C 2013;117:20154–63.
[48] Aubert T, Burel A, Esnault M-A, Cordier S, Grasset F, Cabello-Hurtado F. J Hazard Mater 2012;219:111–8.
[49] Efremova OA, Shestopalov MA, Chirtsova NA, Smolentsev AI, Mironov YV, Kitamura N, et al. Dalton Trans 2014;43:6021–5.
[50] Hsu HC, Shown I, Wei HY, Chang YC, Du HY, Lin YG, et al. Nanoscale 2013;5:262–8.
[51] Loh KP, Bao Q, Eda G, Chhowalla M. Nat Chem 2010;2:1015–24.
[52] Bonaccorso F, Sun Z, Hasan T, Ferrari AC. Nat Photon 2010;4:611–22.
[53] Eda G, Mattevi C, Yamaguchi H, Kim H, Chhowalla M. J Phys Chem C 2009;113:15768–71.
[54] Kumar P, Kumar A, Sreedhar B, Sain B, Ray SS, Jain SL. Chem Eur J 2014;20:6154–61.
[55] Kumar P, Bansiwal A, Bansiwal A, Labhsetwar N, Jain SL. Green Chem 2015;17:1605–9.
[56] Kumar P, Sain B, Jain SL. J Mater Chem A 2014;2:11246–53.
[57] Moon G, Park Y, Kim W, Choi W. Carbon 2011;49:3454–62.
[58] Liang YT, Vijayan BK, Gray KA, Hersam MC. Nano Lett 2011;11:2865–70.
[59] Jiang G, Lin Z, Chen C, Zhu L, Chang Q, Wang N, et al. Carbon 2011;49:2693–701.